Near Surface Geophysics

EAGE
EUROPEAN
ASSOCIATION OF
GEOSCIENTISTS &
ENGINEERS

Electrical resistivity monitoring of an earthslide with electrodes located outside the unstable zone (Pont-Bourquin landslide, Swiss Alps)

Grégory Bièvre[1], Denis Jongmans[1], Thomas Lebourg[2] and Simon Carrière[1]

[1]*Université Grenoble Alpes, Université Savoie Mont Blanc, CNRS, IRD, Université Gustave Eiffel, ISTerre, Grenoble, 38000, France (E-mail: gregory.bievre@univ-grenoble-alpes.fr), and* [2]*Géosciences Azur, CNRS UMR 7329, OCA/Université de Nice, Sophia-Antipolis, 06905, France*

ABSTRACT

In the past decade, passive seismic methods have shown the possibility to detect significant changes in surface wave velocity up to several days prior to landslide failure, even with sensors located outside the unstable zone. Electrical resistivity tomography has also long been used to monitor hydrological changes in landslides. However, the displacement of electrodes relative to each other during landslide movement induces a modification of the geometric factors and, hence, of the apparent resistivity. The first objective of this work is to evaluate the possibility of monitoring the Pont-Bourquin landslide (Swiss Alps) with electrodes located outside the unstable zone. The second objective is to monitor both seismic velocity and electrical resistivity to get insights into the evolution with time of mechanical and hydrological parameters, respectively. The sliding mass was first imaged in three dimensions to produce a resistivity starting model for the further inversion of time-lapse data. Daily time series (235 days from February to November 2015) showed that changes are detected but cannot be spatially localized, in agreement with numerical simulation results. At the seasonal scale, resistivity and seismic time series are positively correlated with temperature and suggest a control by superficial water content. On the scale of a few days, geophysical parameters are negatively correlated with precipitation and suggest rapid infiltration of water into the ground. Although laboratory experiments show that no change in resistivity occurs during fluidization, and since no flow occurred during the monitoring period the evolution of resistivity during a flow event remains an open question.

Key words: Earthslide, Electrical resistivity tomography, Landslide, Monitoring, Resistivity, Seismic.

INTRODUCTION

Electrical resistivity tomography (ERT) has long been used in landslide investigations (Jongmans and Garambois, 2007; Loke *et al*., 2013; Whiteley *et al*., 2019). Apparent resistivity ρ_a is measured using two current-injecting electrodes (labelled A and B) and two further electrodes (labelled M and N) to measure the induced voltage (Telford *et al*., 1990). The apparent resistivity ρ_a (Ω·m) is computed using equation (1):

$$\rho_a = K \cdot R = \frac{2\pi}{\frac{1}{AM} - \frac{1}{BM} - \frac{1}{AN} + \frac{1}{BN}} \cdot \frac{V_{\mathrm{MN}}}{I_{\mathrm{AB}}}, \qquad (1)$$

where K is the geometric factor (m), R is the electrical resistance (Ω), V_{MN} is the voltage (V) measured between electrodes M and N and I_{AB} is the electric current (A) measured between electrodes A and B.

When the method is appropriate for the site conditions, that is with a resistivity contrast sufficient enough between the landslide and the undisturbed ground, the interpretation of inverted resistivity data provides two- and three-dimensional (3D) images of the geological setting and of the landslide

*E-mail: gregory.bievre@univ-grenoble-alpes.fr

geometry (Chambers *et al.*, 2011; Travelletti *et al.*, 2012; Bièvre *et al.*, 2018b; Crawford and Bryson, 2018). When measurements are repeated over time, the method allows the monitoring of changes in resistivity ($\Delta\rho$) (Travelletti *et al.*, 2012; Uhlemann *et al.*, 2017) by measuring changes in the ground resistance ΔR (c.f., equation (2)).

$$\Delta\rho = K \cdot \Delta R. \tag{2}$$

In landslide studies, resistivity variations are generally related to changes in water content and are used to monitor hydrological changes in the sub-surface (for a recent review, see Whiteley *et al.*, 2019). This monitoring approach emerged in the mid- and late-2000s (Lebourg *et al.*, 2005; Jomard *et al.*, 2007; Grandjean *et al.*, 2009) and further applications used either resistivity (Bièvre *et al.*, 2012; Travelletti *et al.*, 2012; Supper *et al.*, 2014; Gance *et al.*, 2016; Uhlemann *et al.*, 2017; Crawford and Bryson, 2018), apparent resistivity (Lebourg *et al.*, 2010; Palis *et al.*, 2017) or electrical resistance (Merritt *et al.*, 2018). In most of these studies, electrical parameters are calibrated with environmental time series (e.g., rainfall, water table level, ground water content, etc.) to provide the evolution of the hydrological process from the surface down to the water table, generally located at a few metres in depth.

Quantitative relationships between resistivity and water content have been established using empirical relationships calibrated in the laboratory (Waxman and Smits, 1968; Yeh *et al.*, 2002; Chambers *et al.*, 2014; Uhlemann *et al.*, 2017). However, electrodes located on the sliding mass move relatively to each other. This induces a change in the geometric factor (ΔK) that was used by Wilkinson *et al.* (2010, 2015) to retrieve electrode displacement at the surface by measuring resistivity variation ($\Delta\rho$). This hypothesis implicitly assumes that the variation in apparent resistivity is related to a change in the geometric factor and not to a modification of the ground porosity and/or water content and, consequently, ground resistance (ΔR; equation (3)):

$$\Delta\rho = \Delta K \cdot R. \tag{3}$$

This potential pitfall was overcome by Uhlemann *et al.* (2015), who geodetically monitored a subset of the installed electrodes to reconstruct the geometry of all the electrodes prior to inverting a 3D dataset. Finally, recent works also showed the possibility to process in time-lapse data with *ad hoc* topography and mesh (and, consequently, geometric factors) for each time sequence (Whiteley *et al.*, 2020) even when the landslide is active. Measuring resistivity in the field is generally quick and efficient. However, the need to determine the

electrode location for each measurement requires the addition of high-resolution geodetic monitoring systems, increasing the cost of the monitoring setup.

This research was motivated by the difficulty of setting up geophysical instruments on landslides that move over several metres/year and that can evolve in mudflows, such as the Pont-Bourquin landslide (PBL) in Switzerland. This landslide has been instrumented and monitored since March 2010, using seismic noise recording with two sensors located on either side of the moving mass (Mainsant *et al.*, 2012; Bièvre *et al.*, 2018a). This setup allowed the detection of a significant drop in surface wave velocity (-7%) in the 8–12 Hz frequency range several days before the occurrence of a mudflow in August 2010 (Mainsant *et al.*, 2012). The dispersion of surface waves was used to deduce the depth of V_s variations. The same experimental setup also revealed low-amplitude reversible velocity variations ($\pm 2\%$) caused by environmental parameters, such as temperature and rainfall (Bièvre *et al.*, 2018a). Due to the interest in obtaining both seismic velocity and electrical resistivity variations on the same site, 36 electrodes were deployed on either side of the unstable zone. The first objective is to test the capacity of an installation with external electrodes to detect resistivity variations in the landslide. The second objective is to compare the changes in mechanical and hydrological parameters (through seismic velocity and electrical resistivity, respectively) to get a better insight into the PBL behaviour. Very little joint geophysical monitoring of landslides has been carried out to date (Grandjean *et al.*, 2009; Bièvre *et al.*, 2012). The main changes in apparent resistivity are expected to come mainly from surface water infiltration. A laboratory study conducted on samples originating from six European landslides, including the PBL, showed that, unlike V_s, electrical resistivity did not show any significant change at the solid–fluid transition (Carrière *et al.*, 2018). In case of the occurrence of a mudflow, the fluidization at the base of the landslide will probably not induce any change in resistivity. The study first focused on obtaining a detailed 3D electrical image of the landslide. In a second step, the capacity of the resistivity method with such a setup (electrodes located outside the unstable zone) to detect resistivity variations in the landslide mass was numerically evaluated. Finally, the time series of resistivity and seismic velocity (235 days) are compared and interpreted in the light of the environmental parameters.

STUDY SITE

The PBL is located in the Swiss Alps (Fig. 1a). This landslide has been active since 2004 and forms part of the larger
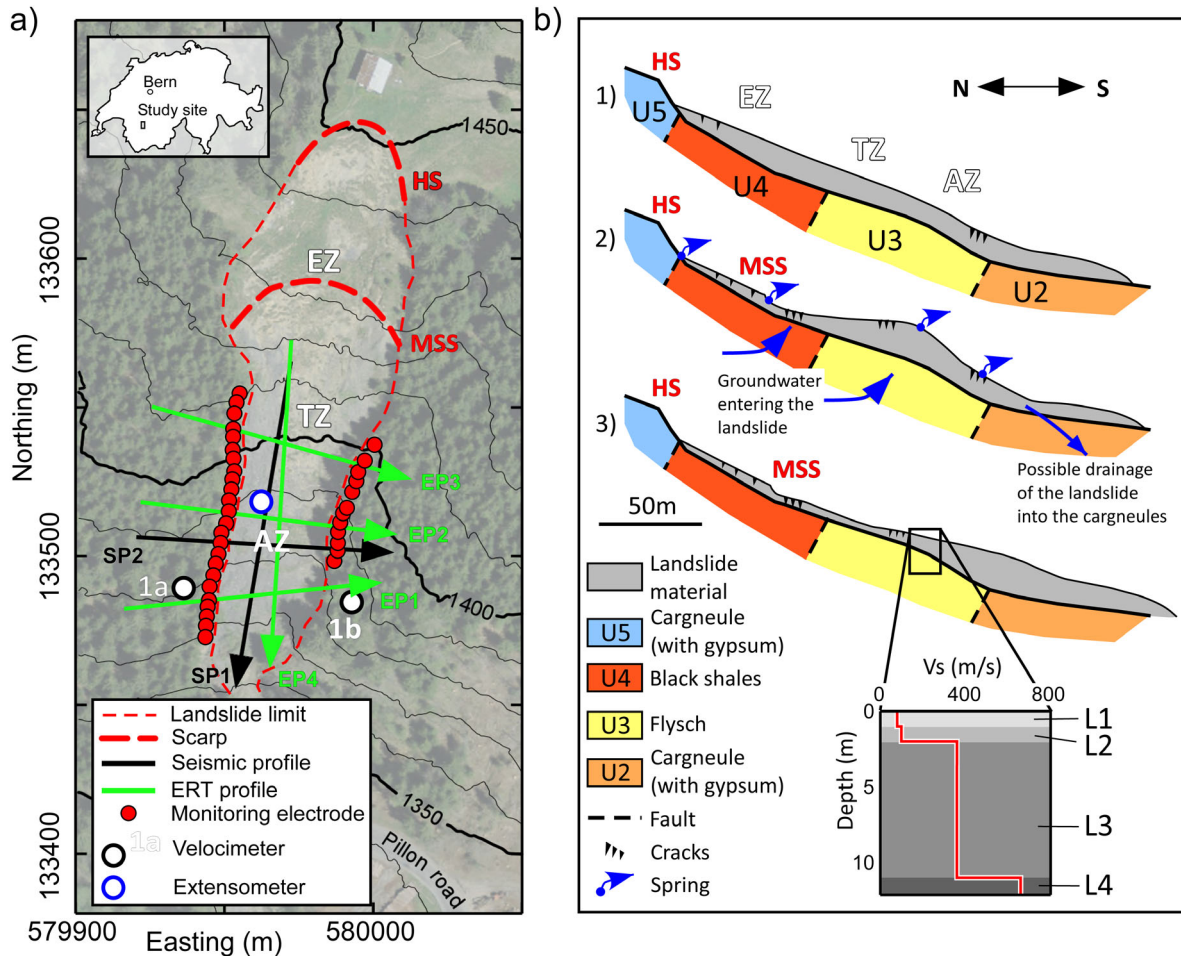
Figure 1 Study site. (a) Location of the Pont-Bourquin landslide (PBL) and of the experiments. Coordinates are metric and expressed in the Swiss grid format. Black lines correspond to topographic contour lines, and elevations are expressed in metres above sea level. Abbreviations: AZ, accumulation zone; EZ, erosion zone; HS, main headscarp; MSS, main secondary scarp; TZ, transportation zone. (1a and 1b): Velocimeters (with the same label) used by Bièvre *et al*. (2018a). (b) Conceptual evolution model of PBL showing three stages: (1) stable state, (2) landslide in the EZ with transportation of material to the AZ, (3) triggering of a debris flow in the AZ after heavy rainfall. The shear-wave velocity (V_s) profile with the different interpreted units (L1 to L4) in the AZ is shown. Figure modified from Mainsant *et al*. (2012) and Bièvre *et al*. (2018a).

Parchets landslide, supposed to have been active since the last glacial retreat (Jaboyedoff et al., 2009). The geological bedrock is made of different lithological units (Triassic cargneules, flyschs and Aalenian black shales; Fig. 1b) separated by thrust faults dipping around 35° towards north. The landslide is a 240-m long and 15–60-m wide translational earthslide with a slight rotational component in its upper part. It presents two main shear surfaces located at around 2 m and 10–11 m in depth (Jaboyedoff et al., 2009). The landslide is made of material originating from the different units, with a predominance of weathered clay originating from the black shales. Detailed presentations of the landslide can be found in Jaboyedoff et al. (2009), Brönnimann (2011)

and Bièvre et al. (2018a). From a hydrogeological point of view, local perched water tables were identified in monitoring wells at shallow depths (1–2 m). These water tables were not identified with geophysical prospecting (P-wave refraction), probably because of experimental setups were not adapted to detect such shallow features (Brönnimann, 2011, see also Section 4.1). The presence of a perennial spring in the lower part of the landslide also suggests that a deep water table exists in the bedrock below the landslide with possible inflow into the landslide.

The PBL moves more or less continuously a few metres/year (Bièvre et al., 2018a; Le Breton et al., 2019). It underwent two flow-like movements in July 2007 ((3–6) × 10³ m³;

Table 1 Acquisition settings and inversion statistical results of geophysical profiles

Profile	Geophysical Parameter	Sensors (#)	Sensor Spacing (m)	Shots (#)	Measurements (#)	Iterations (#)	χ^2	RRMSE (%)
SP1	V_p	24	5	12	187	6	1	4.2
	V_s			5	98	7	1.2	6
SP2	V_p	24	4	9	177	4	0.9	3.5
EP1	ρ	63	1.5		1312	5	0.62	4.7
EP2	ρ	64	1.5		1280	3	1.6	5.1
EP3	ρ	63	1.5		1318	5	0.75	10
EP4	ρ	64	2		1363	9	0.73	7.7
3D	ρ	254	1.5–2		5273	6	0.98	9.8

Abbreviations: RRMSE, relative root-mean-square error; V_p, P-wave velocity; V_s, S-wave velocity; ρ, electrical resistivity.

Jaboyedoff *et al.*, 2009) and August 2010 (a few thousand cubic metres; Mainsant *et al.*, 2012). The mechanism of the PBL is detailed in Bièvre *et al.* (2018a) and can be summarized as follows (Fig. 1b). First, a headscarp is created at the top of the black shales (stage 1). Second, the main secondary scarp is initiated by the faster motion in the central transportation zone, probably resulting from an inflow of groundwater from below the landslide (stage 2 in Fig. 1b). Finally, this results in the accumulation of material in the lower part of the landslide that allows the generation of flows (stage 3).

The seismic monitoring of Rayleigh wave velocity using ambient seismic noise showed a significant drop of up to 7% several days prior to the flow event of August 2010 (Mainsant *et al.*, 2012). The subsequent 4.5 year-long monitoring showed no significant drop in velocity, along with no observed failure (Bièvre *et al.*, 2018a). On the contrary, periodic variations of velocity (period of 1 year) between −2 and +2% were observed during the monitoring period. At the seasonal scale, they were interpreted as resulting from environmental forcing. For shorter periods, decreases in velocity were observed immediately after rainfall and the subsequent infiltration of water into the ground, leading to the decrease of the stiffness of the superficial layers.

MATERIALS AND METHODS

Two seismic profiles labelled SP1 and SP2 (Fig. 1a) were acquired in July 2014 (details are given in Table 1). Compressional (P) and shear (S) waves were recorded with 4.5 Hz vertical and horizontal geophones, respectively, connected to a Geode seismograph. P-waves were generated with a sledgehammer vertically hitting a metallic plate on the ground. S-waves were generated with the same sledge-hammer horizontally hitting a loaded plank oriented perpendicular to the profile. Due to the difficulty to lay the plank along the

slope ($\sim 26°$), S-waves were not acquired along the transverse profile. First-arrival times were manually picked, and the data were inverted using the pyGIMLi package developed by Rücker *et al.* (2017). Inversion results provided satisfactory statistical results (Table 1) in terms of χ^2 and of relative root-mean-square error (RRMSE). The χ^2 parameter is used preferentially to the RRMSE by the pyGIMLi and BERT (see further) packages and reads (Friedel, 2003; Günther *et al.*, 2006)

$$\chi^2 = \frac{1}{n} \sum_{i=1}^{n} \left(\frac{d_i - m_i}{e_i} \right)^2, \tag{4}$$

where n is the number of measurements, i is the rank of the measurement, d_i and m_i are the experimental and theoretical data of rank i, respectively, and e_i is an experimental error. This last encompasses a systematic error (default value of 3%), a measurement error related to the sampling frequency and to the error on the manual picking of first arrivals (on the measured voltage in the case of resistivity) and, finally, an error related to the location of the sensors (0.05 m in this work).

The RRMSE is classically defined as

$$\text{RRMSE}(\%) = \sqrt{\frac{1}{n} \sum_{i=1}^{n} \left(\frac{d_i - m_i}{d_i} \right)^2} \times 100. \tag{5}$$

Four two-dimensional (2D) ERT profiles were acquired in July 2014 (EP1 to EP4; Fig. 1a and details are given in Table 1) with a Terrameter LS resistivimeter using a multigradient configuration (Dahlin and Zhou, 2006). They were inverted individually using the BERT package (Günther *et al.*, 2006; Rücker *et al.*, 2006). They were further gathered to perform a 3D inversion using a mesh constrained with a digital elevation model.

A Syscal Pro Switch resistivimeter was connected to 36 electrodes to monitor the accumulation zone and the lower part of the transportation zone (Fig. 1a). A first test was carried out for several weeks with steel electrodes set into the

ground in a conventional way. The results showed that the contact resistances gradually increased to values up to more than 10 kΩ. On 15 February 2015, 0.3 m long stainless steel electrodes were buried 0.5 m deep to avoid air–water contact and connected to the cables with waterproof connectors. With this layout, the contact resistances remained at 1 kΩ during the 282-day monitoring period ending 23 November 2015. The acquisition system was powered by solar panels connected to a set of batteries, ensuring at least 1 hour of measurements per day. The acquisition system was not remotely controlled, and data were downloaded manually each month. During the monitoring period, 235 daily sequences were actually measured, due to several technical problems resulting from power outages (lightning) and cable breaks (landslide activity, falling trees). Each daily sequence consists of 1654 (half direct and half reciprocal) measurements in an equatorial dipole–dipole configuration (acquisition time ∼1 hour). Each quadrupole measurement was repeated thrice (stack operation) to evaluate repeatability. The time series of apparent resistivity was filtered using thresholds: reciprocity (3%), repeatability (3%), and minimum measured voltage between electrodes M and N (0.01 V). Negative apparent resistivity was also removed. Time-lapse data were inverted into 3D using the BERT package. However, filtering operations lead to variable daily dataset, that is a specific quadrupole is not present in each daily sequence. This discrepancy between the 235 daily measurements prevented the application of classical time-lapse inversions, such as ratio (Schütze *et al.*, 2002) or difference (LaBrecque and Yang, 2001) inversions, which require homogeneous dataset in terms of quadrupoles. It was, therefore, chosen to use a common reference model to process the data in time lapse. The same 3D mesh was used to invert all the time sequences. Several inversion strategies with different starting models were tested and will be described in the Results section. Results were analysed in terms of numeric quality (χ^2, RRMSE) and of coverage.

The 3D finite element modelling was conducted with the Matlab F3DM package (Clément and Moreau, 2016) coupled to the Comsol Multiphysics software to evaluate the ability of the monitoring setup to detect changes and to localize them spatially in the 3D model. The methodology is fully detailed in Bièvre *et al.* (2018c). The geometry and mesh of the model, as well as the resistivity distribution and electrode positions, were defined using Comsol software. The calculation of the voltage at each electrode is handled by a Matlab routine that drives the forward calculation on Comsol. The apparent resistivity data derived for each quadrupole were inverted with the BERT software, using an automatically generated custom mesh, different from the one used to perform the forward calculations. Changes in resistivity were distributed at the surface to simulate the rapid infiltration of rainfall into a top soil layer and also at depth (around 10 m) to simulate the effect of the clay fluidization at the base of the landslide proposed by Mainsant *et al.* (2012).

Temperature time series data available from the site (see further) were used to correct electrical resistivity after inversion to a standard temperature corresponding to the daily average air temperature during the monitoring period (5.6°C). The dependency of resistivity to temperature variations is well known (Hayley *et al.*, 2007, 2010) and is of the form:

$$\rho_{T_{ref}} = \rho_T \cdot (1 + 0.0202 \cdot (T - T_{ref})), \tag{6}$$

where $\rho_{T_{ref}}$ is the resistivity at the reference temperature T_{ref} and ρ_T is the resistivity at temperature T.

The correction factor 0.0202 indicates a 2.02% decrease in resistivity per 1°C increase in temperature and vice versa. However, sub-surface temperatures vary as a function of depth and also as a function of the seasons, according to equations describing heat diffusion such as the relationship proposed by Musy and Soutter (1991):

$$T_{(Z,t)} = T_{mean} + \frac{A}{2} e^{\frac{-Z}{d}} \sin\left(\omega \cdot t + \phi - \frac{Z}{d}\right), \tag{7}$$

where $T_{(Z,t)}$ is the temperature at depth Z for day t, T_{mean} and A are the average air temperature and the difference between the maximum and minimum air temperature measured at a meteorological station, $\omega = 2\pi/365$ is the angular period, ϕ is the offset required to bring air and subsurface temperatures in phase ($\phi = \omega \cdot t_0$, where t_0 is a time lag in days) and d is the depth parameter of the model. Z and t_0 are the two parameters to be evaluated in equation (7). This relationship was used by several authors to correct resistivity values at varying depths (Brunet *et al.*, 2010; Chambers *et al.*, 2014; Uhlemann *et al.*, 2017; Merritt *et al.*, 2018).

The temperature-corrected resistivity values were then divided into four zones according to the position in the landslide (transport and accumulation zones with an N–S limit at the *y*-coordinate = 133,515 m) and the depth (0–5 m and 5–11 m). The average daily resistivity was then computed within each zone. The 3D model, and the four zones, are composed of cells with very different individual volumes (from around 6.5×10^{-4} m^3 at surface close to the electrodes to around 13.6 m^3 at depth) and sensitivities (higher ones are close to the electrodes). Thus, the weighted average resistivity of each

zone was determined using the following equation:

$$\rho_{mean} = \frac{\sum\limits_{i=1}^{n} \rho_i \cdot V_i \cdot S_i}{\sum\limits_{i=1}^{n} V_i \cdot S_i}, \tag{8}$$

where ρ_{mean} is the weighted average resistivity of a zone ($\Omega{\cdot}m$), n is the number of cells of the considered zone, ρ_i ($\Omega{\cdot}m$), V_i (m^3) and S_i (dimensionless) are the resistivity, the volume and the coverage of cell i, respectively.

These four time series were then standardized (subtraction of the mean and normalization by the standard deviation to get zero mean and a variance of 1) and cross-correlated with temperature, precipitation and then with the seismic time series ($\Delta V/V$) computed by Bièvre *et al.* (2018a) between two velocimeters located in the accumulation zone (1a and 1b in Fig. 1a). Cross-correlation C_{X_1,X_2} between two standardized time-series X_1 and X_2 of similar length n and time sampling τ is evaluated using the following equation (among others, Chatfield and Xing, 2019; Paolella, 2019):

$$C_{X_1,X_2}(\tau) = \frac{1}{n}\sum_{t=\tau}^{n} X_1(t) \cdot X_2(t+\tau), \tag{9}$$

where t is the time sample.

Missing data were attributed to a value of zero and did not affect the cross-correlation coefficient cc. The 95% confidence interval CI, inside of which the cross-correlation is considered significantly different from zero, was also computed (see previous references).

Air temperature data were measured at a weather station installed at the rear of the main headscarp. Hourly measurements were averaged to provide daily values. Daily rainfall was obtained from a weather station located in the village of Les Diablerets (~1 km west of the landslide) and operated by the Federal Office of Meteorology and Climatology (MeteoSwiss). Bièvre *et al.* (2018b) showed that using effective rainfall improved hydrogeological interpretations compared to using total rainfall. In the same way, Uhlemann *et al.* (2017) also used effective rainfall to interpret resistivity time series on the Hollin Hill landslide in England. Unfortunately, it was not possible to evaluate effective rainfall on the study site because of the relevant parameters were not available, namely the solar radiation. Surface displacements were measured using an extensometer installed in the accumulation zone (location in Fig. 1a). Snow accumulating on the extensometer wire and trees damaging the same wire generated several gaps in the data.
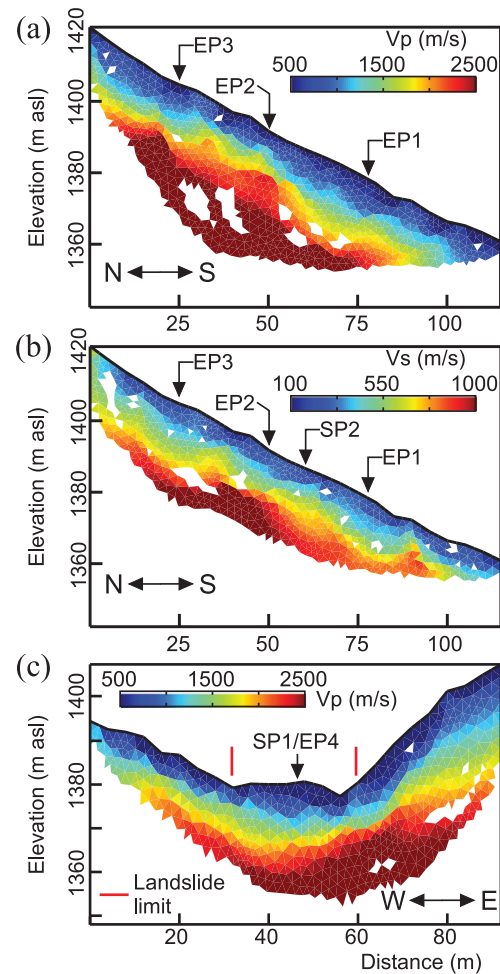

Figure 2 Seismic refraction tomography results. (a) P-wave velocity along profile SP1. (b) S-wave velocity along profile SP1. (c) P-wave velocity along profile SP2. The location of the profiles is shown in Fig. 1(a).

RESULTS

Two- and three-dimensional geophysical images

The 2D seismic tomography SP1, which is located along the landslide, shows a seismic stratification parallel to the slope for both P-waves (Fig. 2a) and S-waves (Fig. 2b). Both images present low velocities over the first 10 m below the surface (<800 m/s and <300 m/s for V_p and V_s, respectively). Below 10 m, V_p and V_s increase up to more than 2500 m/s and 1000 m/s, respectively. The depth of 10 m matches previous findings of Mainsant *et al.* (2012) and corresponds to the interface between the landslide and the Jurassic bedrock. The P-wave velocity in the landslide also reveals that the body of the landslide was likely not saturated during measurements
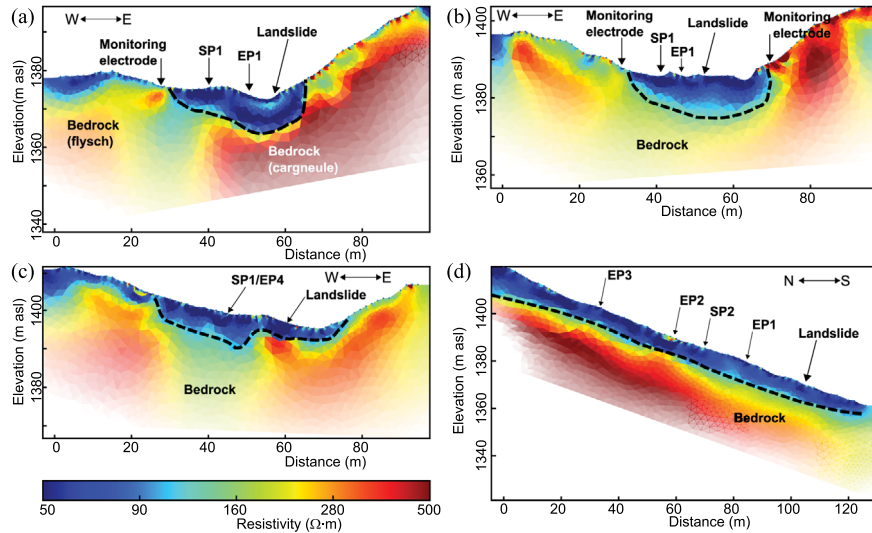
Figure 3 2D electrical resistivity tomography images along profiles: (a) EP1 (accumulation zone), (b) EP2 (accumulation zone), (c) EP3 (transportation zone) and (d) EP4. The location of the profiles is shown in Fig. 1(a).

(July 2014). Profile SP2 (Fig. 2c) was conducted across the landslide in the accumulation zone (see location in Fig. 1a). It shows P-wave velocity comparable to SP1 ($V_p < 800$ m/s in the first 10 m and up to more than 2500 m/s below this depth). However, the low-velocity layer is observed throughout the profile, suggesting that the subsurface is loose and preventing a clear delineation of the landslide body from the stable zone.

ERT profiles EP1 (Fig. 3a) and EP2 (Fig. 3b) were conducted across the accumulation zone. They show a clearly delineated low-resistivity zone in the centre of the profile ($\rho < 100\,\Omega\cdot$m) with a maximum thickness of around 10 m and a width of 25–30 m. This layer corresponds to the landslide. Below, the bedrock shows higher resistivity ($\rho > 150\,\Omega\cdot$m and up to more than 500 $\Omega\cdot$m). The EP3 profile (Fig. 3c) carried out across the transportation zone also reveales the body of the landslide ($\rho < 100\,\Omega\cdot$m), with a slightly shallower depth (8–10 m). The extension of the low–resistivity layer to the west probably corresponds to another landslide located west of the PBL (Jaboyedoff *et al.*, 2009). Profile EP4 was performed along the landslide (Fig. 3d) and shows an average thickness of the landslide body of about 7 m. In contrast to the seismic images, ERT profiles then provide a very good distinction between landslide and bedrock.

EP1 to EP4 were then gathered and inverted in 3D. The inversion converged after a few iterations with $\chi^2 \sim 1$ and RRMSE $\sim 10\%$ (Fig. 4 and Table 1). The landslide body is well detected with a low resistivity of 75–80 $\Omega\cdot$m (Fig. 4a), while the resistivity of the bedrock is slightly higher in the accumulation zone (150–170 $\Omega\cdot$m) than in the transport zone (120

$\Omega\cdot$m; Fig. 4b). This variation is probably due to the difference in bedrock lithology, with the presence of flysch in the accumulation zone and the predominance of black shales in the transport zone (Fig. 1b). One-dimensional (1D) resistivity–depth curves were extracted from the 3D model and show that the landslide presents an average thickness of 10 m (Fig. 4b), in agreement with the shear-wave velocity (V_s) profile of Mainsant *et al.* (2012) located at the intersection between EP2 and EP4 and shown in Fig. 4(b). The volume of the landslide imaged below the main secondary scarp and deduced from the 3D model is of 22.5×10^3 m^3. Finally, the 1D resistivity profiles extracted from the 2D images EP1 and EP3 (Fig. 4c) show that the landslide–bedrock interface is located at around 10 m depth. The 2D resistivity in the landslide ($\sim$50 Ω.m) is lower than in the 3D image. For the bedrock, the resistivity is globally similar below EP3, but is up to more than 350 $\Omega\cdot$m below EP1, compared to $\sim$150–170 $\Omega\cdot$m obtained with 3D inversion.

Numerical study

The landslide geometry at depth for numerical modelling has been extracted from seismic and ERT profiles. For simplification purposes, the topography was removed. The numerical model (Fig. 5a) with a volume of $\sim$26 $\times$ 10^6 m^3 contains $\sim$254 $\times$ 10^3 tetrahedrons connected by 49 $\times$ 10^3 nodes. The resistivity of the bedrock and of the landslide was set to 150 and 75 $\Omega\cdot$m, respectively, based on results from the previous section. A 1-m thick layer was placed at the base of the

Figure 4 3D electrical resistivity tomography (a) 3D image of the PBL below the main secondary scarp. (b) 1D resistivity–depth curves extracted from the 3D model and comparison with the shear-wave velocity profile from Mainsant *et al.* (2012). The colours of the curves refer to their location in Fig. 4(a). (c) 1D resistivity–depth curves extracted from 2D models EP1 (light orange) and EP3 (green).
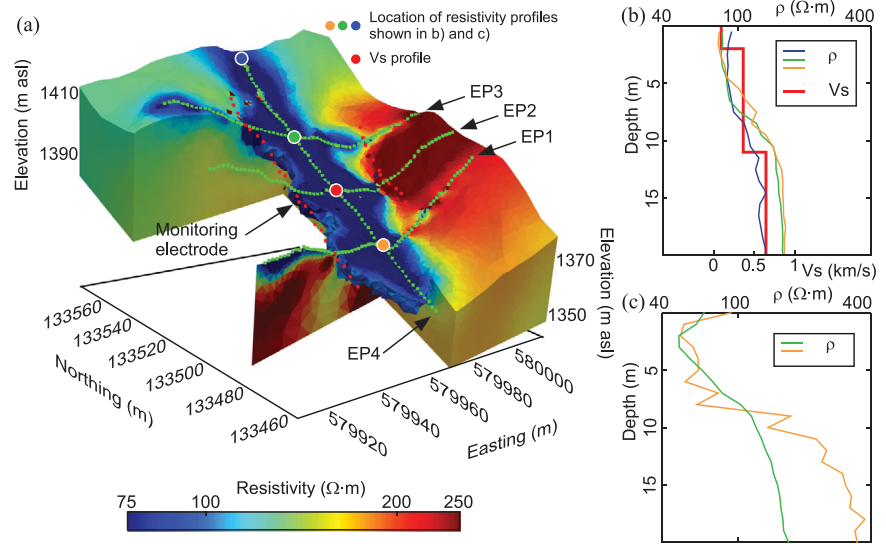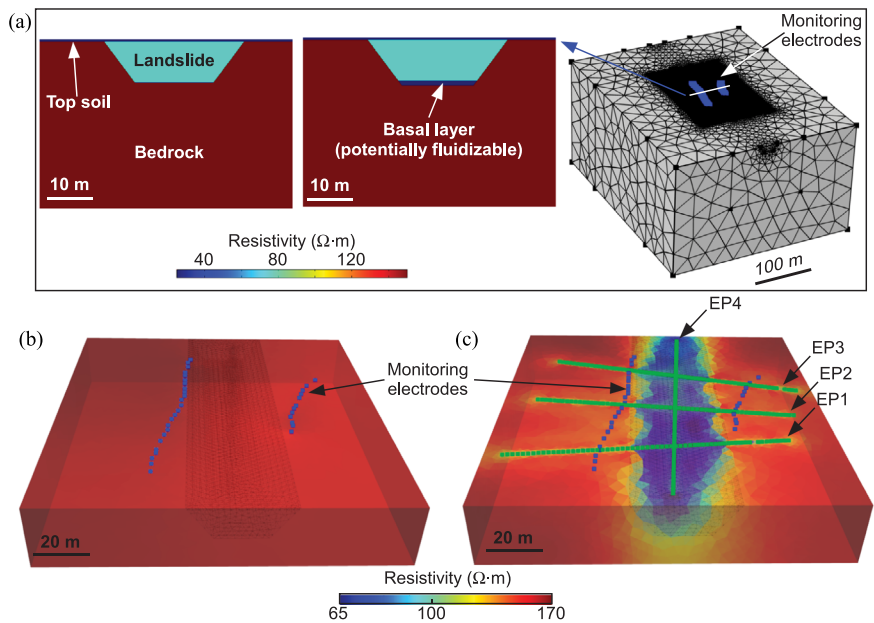

Figure 5 Numerical study. (a) Computation domain. (b) Inversion result without a starting model. (c) Inversion result using a starting model.

landslide to test the ability of the monitoring setup to detect resistivity changes at depth (75 or 25 Ω·m). Finally, a 0.5-m thick layer was placed at the surface to mimic a decrease in resistivity following rainfall and water infiltration in the subsurface (75 or 25 Ω·m).

Four cases were studied, and they are detailed in Table 2. First, the ability of the monitoring system to retrieve the geometry of the sub-surface was tested. A model comprising a layer with resistivity $\rho = 75$ Ω·m, including the landslide, the surface soil and the basal layer, and the bedrock ($\rho = 150$ Ω·m),

was used to calculate the theoretical apparent resistivity values (case 1 of Table 2). Using this simple model, a first simulation was conducted using the 36 monitoring electrodes only and inversion results are presented in Fig. 5(b). The resistivity values remain in a narrow range between 150 and 175 Ω·m, and the statistical results are not satisfactory ($\chi^2 \sim 1$ and RRMSE > 40%). These results indicate that the monitoring system alone cannot retrieve the correct distribution of resistivity in space and at depth. A second simulation was conducted in two steps using the same model (case 1). First,

Table 2 The four cases studied with numerical simulation

Unit	Resistivity (Ω·m)			
	Case 1	Case 2	Case 3	Case 4
Landslide	75	75	75	75
Bedrock	150	150	150	150
Top soil	75	25	25	75
Basal layer	75	75	25	25

synthetic apparent resistivity values were computed for profiles EP1 to EP4. They were gathered and inverted in 3D. The resulting model ($\chi^2 \sim 1$ and RRMSE < 5%) was then used as a starting model to invert the data computed with the monitoring system. The resistivity image ($\chi^2 \sim 1$ and RRMSE < 5%) is presented in Fig. 5(c). The landslide is fairly well detected with a resistivity of around 80 Ω·m. The volume of the landslide retrieved from 3D ERT in Fig. 5(c) is $25 \times 10^3 \mathrm{m}^3$, compared to the original volume of the landslide in the model (Fig. 5a) of $30.5 \times 10^3 \mathrm{m}^3$. Despite this slight underestimation of 15%, the use of a start model with a good resolution enhances the results of the inversion with the monitoring setup only. This approach will be used for further inversions.

Second, changes in resistivity were introduced in the model in the top soil and in the basal layer (Fig. 5a and Table 2). The 1-m thick layer at the base of the landslide was changed from 75 Ωm to 25 Ω·m to simulate a strong increase in water content, potentially leading to the fluidization of this layer (Mainsant *et al.*, 2012, 2015). Another change was brought to the model, in the top soil layer (from 75 Ωm to 25 Ω·m), to simulate water infiltration following rainfall. These two modifications lead to four potential combinations (models) presented in Table 2. They were computed, and the resulting theoretical data were inverted using the 3D model previously established as a starting model. Inversion results are satisfactory ($\chi^2 \sim 1$ and RRMSE < 5%), and 1D profiles extracted at the intersection between EP2 and EP4 (see, Fig. 5c for location) are shown in Fig. 6. Globally, the four models lead to the same inverted results. All curves present the strongest resistivity gradient at 10 m depth, which corresponds to the limit between the landslide and the bedrock. A decrease in resistivity at the surface and/or at depth induces after inversion a global shift of the resistivity profile towards lower values over the entire depth, which makes it impossible to locate the resistivity variations. These results suggest that the experimental monitoring device is not capable of detecting localized variations on the surface or at depth, but rather will provide integrative volumetric information on resistivity variations.
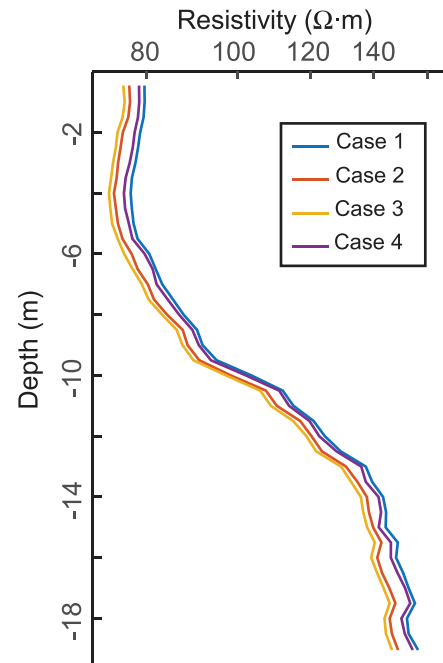

Figure 6 1D resistivity profiles of numerical simulations for four resistivity configurations. The details of the geophysical parameters are presented in Table 2.
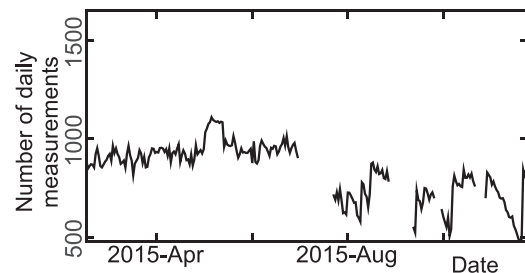

Figure 7 Daily measurements available during the 282 days of the survey after filtering of apparent resistivity data.

Four-dimensional electrical resistivity tomography

Four-dimensional electrical resistivity tomography time series

The number of daily apparent resistivity measurements remaining after filtering operations is shown in Fig. 7. From the 282 days of the survey with 1654 direct and reciprocal measured quadrupoles, the daily available dataset comprises 235 sequences with 900–1000 quadrupoles from February up to July 2015 and around 500–800 quadrupoles after July 2015. This relatively low number of daily quadrupoles can be explained by the low thresholds that were used in this work (3% reciprocity and repeatability, minimum measured voltage of 0.01 V), lower than those used in other studies (e.g., Uhlemann

Figure 8 4D inversion statistical results and analysis for the four starting models (see the text for details). (a) Inversions statistical results. RRMSE: relative root-mean-square error. (b) Coverage for the 2D EP2 profile of Fig. 3(b). (c) Coverage of 3D models (first day of monitoring) with different starting models. The first day of monitoring was chosen for the figure since variations during the monitoring period are moderate.
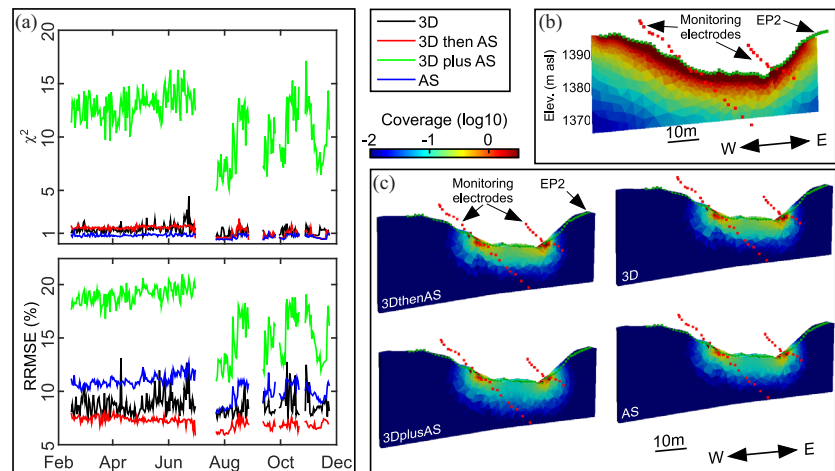
et al., 2017, with a reciprocity threshold of 10%). However, in this work, the large distance between the two flanks of the landslide induces large geometric factors associated with potential low signal-to-noise ratios. It was then decided to keep only robust apparent resistivity measurements.

Daily quadrupoles were then inverted, and four strategies with varying starting models were tested to obtain the highest possible coverage. The first starting model was the 3D model of Fig. 4 (i.e., the result of the 3D inversion of profiles EP1 to EP4) and is referred to as '3D'. The second starting model consisted in using '3D' as a starting model to invert the average sequence ('AS') of the 235 daily sequences dataset, and the resulting model was used as a starting model for the inversion of the daily sequences. This starting model is referred to as '3DthenAS'. The third starting model was the model resulting from the joint inversion of profiles EP1 to EP4 and the average monitoring sequence. It is referred to as '3DplusAS'. Finally, the fourth starting model consisted of the average monitoring sequence only and is referred to as 'AS'. The same mesh was used to invert all data. Figure 8(a) shows the statistical results of inversions. Models '3D', '3DthenAS' and 'AS' exhibit satisfactory statistics with $\chi^2 \sim 1$ and RRMSE < 12%. On the contrary, it was not possible to obtain satisfactory values for the starting model '3DplusAS' (χ^2 ranging between 10 and 20 and RRMSE between 12% and 20%). Results were then analysed in terms of coverage. Figure 8(b, c), presents the sensitivity along profile EP2 and along the cross sections extracted from the 3D models at the same location and for the first day of monitoring, respectively. These figures show first a very much lower coverage for 3D time-lapse inversion compared to 2D imaging. They also reveal that most of the coverage is located around the electrodes and, to a minor extent, to the landslide body. The four models provided globally similar coverage, with slightly higher values for models '3DthenAS' and '3D'. Since '3DthenAS' and '3D' provided similar χ^2 (~1), the model providing the lowest RRMSE, namely '3DthenAS', will be used for further analysis.

Temperature correction

Prior to further processing, inverted resistivity was normalized to a common temperature. Unfortunately, no sub-surface temperature data were acquired during the monitoring period. However, sub-surface and aerial temperature data are available in 2011 and 2012. These time series were used to evaluate separately the parameters of equation (7) and, in particular, the characteristic depth d, which is characteristic of the site. Figure 9(a) presents the experimental aerial and sub-surface temperature time series measured on the site between January 2011 and January 2013 and used to fit equation (5). From experimental data with sensors at depths of 1.35 m and 2.25 m (Fig. 9b, c, respectively), the following parameters were obtained: $T_{mean} = 8.1°$ and $A = 33.05°$. The separate evaluation of parameters d and t_0 provided similar values $d = 1.5$ m and $t_0 = 24$ days. Parameter d previously determined was integrated to equation (7). Then the only parameter left do determine was the time lag t_0 during the ERT-monitoring period (Fig. 9d). The following parameters were obtained from the meteorological station: $T_{mean} = 5.6°$, $A = 27.3°$. From the fitting, the value of t_0 was found to be 65 days. The temperature curves computed at four depths are shown in Fig. 9(d). They suggest that the temperature effect on resistivity becomes
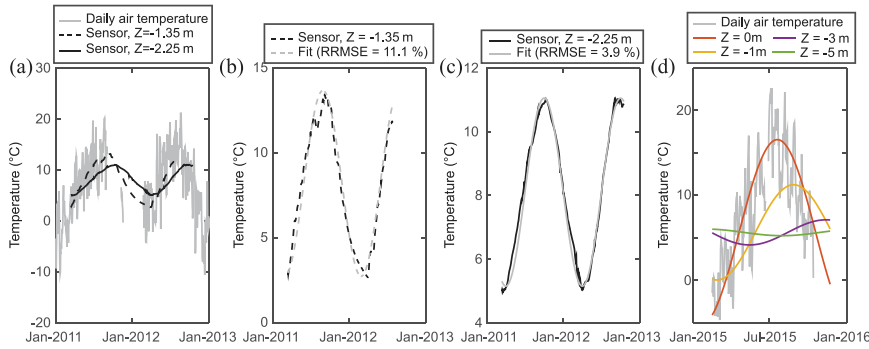
Figure 9 Evaluation of sub-surface temperature. (a) Experimental surface and sub-surface temperatures. (b) Fit of experimental data at a depth of 1.35 m. (c) Fit of experimental data at a depth of 2.25 m. (d) Evaluation of sub-surface temperatures at four depths during the ERT-monitoring period.
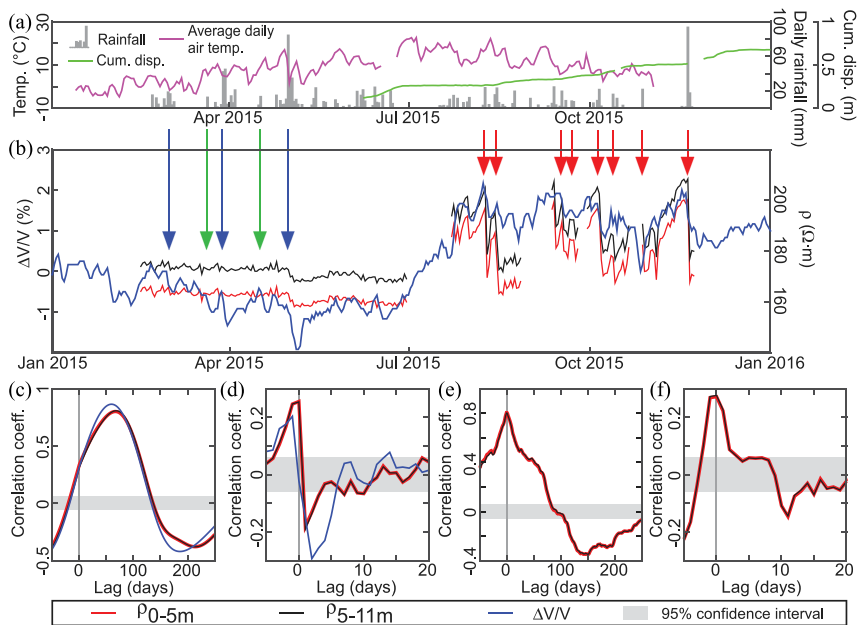

Figure 10 Resistivity, seismic velocity and rainfall time-series analysis. (a) Average daily air temperature, daily precipitation and daily cumulative displacement. (b) Resistivity and relative seismic velocity time series. Red, green and blue arrows indicate precipitation-related events. Green arrows indicate small rain events (< 15 mm) followed by a drop in seismic velocity but no change in resistivity. Blue (resp. red) arrows indicate a small (resp. pronounced) drop in seismic velocity and resistivity in winter and spring (resp. summer and autumn). (c) Correlograms of unfiltered resistivity and seismic velocity with temperature. (d) Correlograms of high-pass filtered (corresponding period of 30 days) time series of resistivity and seismic velocity with precipitation. (e) Correlograms of unfiltered resistivity with seismic velocity in the two zones. (f) Correlograms of high-pass filtered (corresponding period of 30 days) resistivity with seismic velocity.

limited for depths greater than 5 m. Resistivity values were then standardized to T_{mean} using equation (4).

Analysis of time series

As explained in Section 3, the time series analysis was conducted by splitting the landslide body in four zones (the two transport zone TZ and accumulation zone AZ, at two depth ranges 0–5 and 5–11 m). As similar results were obtained for AZ and TZ, only results of the accumulation zone will be further presented (Fig. 10). At the seasonal scale (environmental and displacement time series are shown in Fig. 10a), the two time series of resistivity and $\Delta V/V$ show a similar evolution (Fig. 10b). The values decrease from February 2015, reach a minimum in May and June, and then increase until the end of November. These observations indicate lower resistivity in

winter and spring, in relationship with a shallower water table and a higher water content in the vadose zone during these seasons. On a shorter timescale, the time series show rapid responses of both geophysical parameters to rainfall. This is highlighted by the blue and red arrows in Fig. 10(b), which exhibit a decrease in resistivity and seismic velocity following precipitation events. However, it is observed that small precipitation events (< 15 mm per day) in winter and spring induce a drop in $\Delta V/V$ but not in resistivity (green arrows in Fig. 10b). In addition, a drop in resistivity appears to be greater in summer and autumn (red arrows) than in winter and spring (blue arrows). This could be related to widely open cracks in summer and autumn (Bièvre *et al.*, 2018a) that favour water infiltration following precipitation. Longer time series, however, are required to confirm this observation and hypothesis. However, this observation is in agreement with findings of Merritt

et al. (2018) on the Hollin Hill clayey landslide in England. They observed increases in temperature-corrected electrical resistance during summer periods. This increase was interpreted as resulting from desiccation and cracking. Intense periods of rainfall were followed by a rapid drop in electrical resistance that was interpreted as caused by the annealing of cracks and the increase of soil water content in the very shallow subsurface.

At the seasonal scale, resistivity and $\Delta V/V$ time series are significantly (*cc* values between 0.80 and 0.85) and positively correlated with temperature (Fig. 10c) with lags of 68 days ($\rho_{0-5\,m}$ and $\rho_{5-11\,m}$) and 60 days ($\Delta V/V$). Merritt *et al.* (2018) observed similar lags (∼1.5 month) with temperature uncorrected electrical resistance (median depth of investigation of around 1.9 m). In this work, the increase of temperature-corrected resistivity is attributed to a decrease of water content, which is itself caused by an increase in evapotranspiration originating from an increase in temperature. The similar lags suggest that, in the present study and given the experimental setup, resistivity is mainly sensitive to shallow variations.

Time series were then high-pass filtered (corresponding period of 30 days) to focus on short-term effects and cross-correlated with precipitation. The curves (Fig. 10d) show a negative correlation with a rapid reaction of resistivity ($\rho_{0-5\,m}$ and $\rho_{5-11\,m}$) to precipitation. The correlation coefficient *cc* exhibits a minimum (− 0.19) for a lag of 1 day, with a further rapid increase and no significant effect for durations greater than 3 days after precipitation. The seismic correlogram is comparable with a negative correlation reaching a minimum (*cc* = − 0.29) for a lag of 2 days and a further increase to non-significant *cc* for lags greater than 5 days. The comparable reaction of each resistivity depth range to precipitation underlines the low ability of the monitoring system to localize resistivity changes at depth. It confirms numerical results and indicates that resistivity measurements in this work provide an information that must be considered global at the scale of the landslide.

The cross-correlation of unfiltered resistivity with $\Delta V/V$ exhibits a maximum *cc* of 0.8 for the two resistivity curves (Fig. 10e) for a lag of 0 days, mimicking auto-correlation curves. This highlights a high similarity between resistivity and $\Delta V/V$ curves, which is clearly visible on the time series in Fig. 10(b). These results suggest that these two geophysical parameters react simultaneously to environmental forcing at the seasonal scale. The same analysis was conducted with high-pass filtered time series (corresponding period of 30 days) to study the correlation for short-term events. Results (Fig. 10f) show moderate but significant (*cc* = 0.27) positive peaks of

correlation at zero lag with a subsequent rapid decrease to non-significant values for lags greater than 2 days. These results indicate a similar reaction of both geophysical parameters with decreases in resistivity and seismic velocity rapidly following short-term events such as precipitation. Once again, this can be observed on the time series (arrows in Fig. 10b). Finally, these results suggest that the geophysical parameters are better correlated at the seasonal scale that at the short-term scale.

To conclude, this analysis shows a similar reaction of the two geophysical parameters to both seasonal and short-term environmental parameter variations, suggesting a common control factor. On a seasonal scale, the increase in resistivity and in $\Delta V/V$ in spring and summer suggests a decrease in water content and an increase in rigidity (in parallel with a decrease in wet density) in the superficial layer. This results from the continuous increase in evapotranspiration caused by the increase in temperature. In autumn and winter, there is an inverse relationship with the constant drop in temperature. In the short term, precipitation generates a decrease in resistivity and seismic velocity due to the infiltration of water into the ground, but with a different behaviour depending on the season. In summer and autumn, rainfall is immediately followed by a significant drop in resistivity; while in winter and spring, only heavy rainfall or snowmelt causes a decrease in resistivity. This could be interpreted as the result of cracks much more widely open in summer and autumn because of shrinkage, and thus favouring water infiltration at depth, as already suggested on other landslides (Bièvre *et al.*, 2012; Travelletti *et al.*, 2012; Merritt *et al.*, 2018). The behaviour is illustrated in Fig. 11(a, b) for winter/spring (limited infiltration through cracks) and summer/autumn (higher amount of infiltration through cracks), respectively, with seasonal variations in shear-wave velocity and electrical resistivity as a function of depth illustrated in Fig. 11(c).

SYNTHESIS AND CONCLUSIONS

The Pont-Bourquin landslide was imaged using 2D seismic and 3D resistivity tomography. The 3D image confirmed previous investigation with average width and depth of around 40 and 10 m, respectively. A setup with electrodes located in the stable zone was used to detect resistivity variations in the landslide, similar to what was done previously with seismic sensors to reveal velocity variations $\Delta V/V$. An extensive numerical study using the 3D landslide electrical model was performed to test the sensitivity of the measurements to resistivity changes in the landslide. These changes are detected
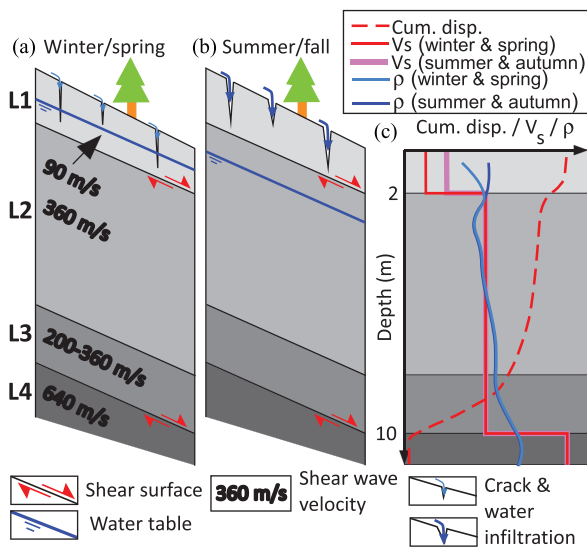
Figure 11 Slope deformation model of the Pont-Bourquin landslide, modified from Bièvre *et al*. (2018a). (a) Sketch in winter and spring with a shallow water table and clogged fissures. (b) Sketch in summer and autumn with a deeper water table and widely open cracks allowing rapid water infiltration. (c) Measured geophysical parameters (V_s, ρ) and conceptual cumulative displacement profile (cum. disp.).

by the external electrodes, but cannot be spatially localized, even though the structure of the landslide is well known. The results of the time-lapse experiment of 235 days conducted with that setup show that $\Delta V/V$ and resistivity time series have a similar shape and are therefore driven by the same environmental parameters. At the seasonal scale, $\Delta V/V$ and resistivity are positively correlated to temperature with zero lag, suggesting a seasonal water content variation is predominantly controlled by temperature. On a scale of a few days, $\Delta V/V$ and resistivity are moderately and negatively correlated to rainfall with time lags of a few days, indicating rapid infiltration of water into the ground. The drop in resistivity that follows rainfall appears stronger in summer and autumn, suggesting a higher amount of infiltration through more widely open fissures and cracks because of shrinkage. Regardless of the timescale, most of the geophysical variations measured during this experiment therefore probably come from water content changes in the upper layer. Despite the low resolution of the electrical-monitoring system, it showed an overall good agreement with velocity variations. Since wireless transmission of data is generally not an issue anymore, the two geophysical parameters could be jointly used to provide hydrological and mechanical information on potential precursors to the deformation of slow-moving landslides. Finally, and although laboratory experiments indicate that the electrical resistivity

does not vary during clay fluidization, the evolution of electrical resistivity before and during a mudflow such as the August 2010 event that generates a precursory drop of 7% in $\Delta V/V$ remains an open question.

ACKNOWLEDGEMENTS

DATA AVAILABILITY STATEMENT

Data are available upon reasonable request from the corresponding author.

CONFLICT OF INTEREST

The authors declare they have no conflict of interest.

ORCID

Grégory Bièvre (iD) https://orcid.org/0000-0002-6382-2824

REFERENCES

Bièvre, G., Jongmans, D., Winiarski, T. and Zumbo, V. (2012) Application of geophysical measurements for assessing the role of fissures in water infiltration within a clay landslide (Trièves area, French Alps). *Hydrological Processes*, 26(14), 2128–2142. https://doi.org/10.1002/hyp.7986.

Bièvre, G., Franz, M., Larose, E., Jongmans, D., Jaboyedoff, M. and Carrière, S. (2018a) Influence of environmental parameters on seismic velocity variations in a clayey mudflow (Pont-Bourquin, Switzerland). *Engineering Geology*, 245, 248–257. https://doi.org/10.1016/j.enggeo.2018.08.013.

Bièvre, G., Joseph, A. and Bertrand, C. (2018b) Preferential water infiltration paths in a clayey earthslide evidenced by cross-correlation of hydrometeorological time series (Charlaix, French Western Alps). *Geofluids*, 20(9593267). https://doi.org/10.1155/2018/9593267. Special issue "The Role and Impact of Geofluids in Geohazards".

Bièvre, G., Oxarango, L., Günther, T., Goutaland, D. and Massardi, M. (2018c) Improvement of 2D ERT measurements conducted along a small earth-filled dyke using 3D topographic data and 3D computation of geometric factors. *Journal of Applied Geophysics*, 153, 100–112. https://doi.org/10.1016/j.jappgeo.2018.04.012.

Brönnimann, C. (2011) *Effect of groundwater on landslide triggering*. PhD thesis, École Polytechnique Fédérale de Lausanne, Switzerland.

Brunet, P., Clément, R. and Bouvier, C. (2010) Monitoring soil water content and deficit using electrical resistivity tomography (ERT) – a case study in the Cévennes

area, France. *Journal of Hydrology*, 380(1–2), 146–153. https://doi.org/10.1016/j.jhydrol.2009.10.032.

Carrière, S., Bièvre, G., Jongmans, D., Chambon, G., Bellot, H. and Lebourg, T. (2018) Measurement of geophysical parameters on clay samples at the solid-fluid transition. *Near Surface Geophysics*, 16(1), 1–15. https://doi.org/10.3997/1873-0604.2017039.

Chambers, J., Wilkinson, P., Kuras, O., Ford, J.R., Gunn, D.A., Meldrum, P., Pennington, C.V.L., Weller, A.L., Hobbs, P.R.N. and Ogilvy, R.D. (2011) Three-dimensional geophysical anatomy of an active landslide in Lias Group mudrocks, Cleveland basin, UK. *Geomorphology*, 125, 472–484. https://doi.org/10.1016/j.geomorph.2010.09.017.

Chambers, J.E., Gunn, D.A., Wilkinson, P.B., Meldrum, P.I., Haslam, E., Holyoake, S., Kirkham, M., Kuras, O., Merritt, A. and Wragg, J. (2014) 4D electrical resistivity tomography monitoring of soil moisture dynamics in an operational railway embankment. *Near Surface Geophysics*, 12(1), 61–72. https://doi.org/10.3997/1873-0604.2013002.

Chatfield, C. and Xing, H. (2019) *The Analysis of Time Series. An Introduction with R*, 7th edition. Texts in Statistical Science. CRC Press/Chapman & Hall.

Clément, R. and Moreau, S. (2016) How should an electrical resistivity tomography laboratory test cell be designed? Numerical investigation of error on electrical resistivity measurement. *Journal of Applied Geophysics*, 127, 45–55. https://doi.org/10.1016/j.jappgeo.2016.02.008.

Crawford, M.M. and Bryson, L.S. (2018) Assessment of active landslides using field electrical measurements. *Engineering Geology*, 233, 146–159. https://doi.org/10.1016/j.enggeo.2017.11.012.

Dahlin, T. and Zhou, B. (2006) Multiple-gradient array measurements for multichannel 2D resistivity imaging. *Near Surface Geophysics*, 4(2), 113–123.

Friedel, S. (2003) Resolution, stability and efficiency of resistivity tomography estimated from a generalized inverse approach. *Geophysical Journal International*, 153(2), 305–316. https://doi.org/10.1046/j.1365-246X.2003.01890.x.

Gance, J., Malet, J.-P., Supper, R., Sailhac, P., Ottowitz, D. and Jochum, B. (2016) Permanent electrical resistivity measurements for monitoring water circulation in clayey landslides. *Journal of Applied Geophysics*, 126, 98–115. https://doi.org/10.1016/j.jappgeo.2016.01.011.

Grandjean, G., Hibert, C., Mathieu, F., Garel, E. and Malet, J.-P. (2009) Monitoring water flow in a clay-shale hillslope from geophysical data fusion based on a fuzzy logic approach. *Comptes Rendus Geosciences*, 341(10–11), 937–948. https://doi.org/10.1016/j.crte.2009.08.003.

Günther, T., Rücker, C. and Spitzer, K. (2006) Three-dimensional modelling and inversion of DC resistivity data incorporating topography – II. Inversion. *Geophysical Journal International*, 166(2), 506–517. https://doi.org/10.1111/j.1365-246X.2006.03011.x.

Hayley, K., Bentley, L.R., Gharibi, M. and Nightingale, M. (2007) Low temperature dependence of electrical resistivity: implications for near surface geophysical monitoring. *Geophysical Research Letters*, 34, L18402. https://doi.org/10.1029/2007GL031124.

Hayley, K., Bentley, L.R. and Pidlisecky, A. (2010) Compensating for temperature variations in time-lapse electrical resistivity difference imaging. *Geophysics*, 75(4), WA51–WA59. https://doi.org/10.1190/1.3478208.

Jaboyedoff, M., Pedrazzini, A., Loye, A., Oppikofer, T., Güell, I., Pons, M. and Locat, J. (2009) Earth flow in a complex geological environment: the example of Pont Bourquin, Les Diablerets (Western Switzerland). In: Malet, J.-P., Remaître, A. and Bogaard, T.A. (Eds.) *Landslide Processes, from Geomorphologic Mapping to Dynamic Modelling*, CERG edition. Strasbourg, France: European Centre on Geomorphological Hazards, pp. 131–137.

Jomard, H., Lebourg, T., Binet, S., Tric, E. and Hernandez, M. (2007) Characterization of an internal slope movement structure by hydrogeophysical surveying. *Terra Nova*, 19(1), 48–57. https://doi.org/10.1111/j.1365-3121.2006.00712.x.

Jongmans, D. and Garambois, S. (2007) Geophysical investigation of landslides: a review. *Bulletin de la Société Géologique de France*, 178(2), 101–112. https://doi.org/10.2113/gssgfbull.178.2.101.

LaBrecque, D.J. and Yang, X. (2001) Difference inversion of ERT data: a fast inversion method for 3-D in situ monitoring. *Journal of Environmental and Engineering Geophysics*, 6(2), 83–89. https://doi.org/10.4133/JEEG6.2.83.

Le Breton, M., Baillet, L., Larose, E., Rey, E., Benech, P., Jongmans, D., Guyoton, F. and Jaboyedoff, M. (2019) Passive radio-frequency identification ranging, a dense and weather-robust technique for landslide displacement monitoring. *Engineering Geology*, 250, 1–10. https://doi.org/10.1016/j.enggeo.2018.12.027.

Lebourg, T., Binet, S., Tric, E., Jomard, H. and El Bedoui, S. (2005) Geophysical survey to estimate the 3D sliding surface and the 4D evolution of the water pressure on part of a deep seated landslide. *Terra Nova*, 17(5), 399–406.

Lebourg, T., Hernandez, M., Zerathe, S., El Bedoui, S., Jomard, H. and Fresia, B. (2010) Landslides triggered factors analysed by time lapse electrical survey and multidimensional statistical approach. *Engineering Geology*, 114(3–4), 238–250. https://doi.org/10.1016/j.enggeo.2010.05.001.

Loke, M.H., Chambers, J.E., Rucker, D.F., Kuras, O. and Wilkinson, P.B. (2013) Recent developments in the direct-current geoelectrical imaging method. *Journal of Applied Geophysics*, 95, 135–156. https://doi.org/10.1016/j.jappgeo.2013.02.017.

Mainsant, G., Larose, E., Brönnimann, C., Jongmans, D., Michoud, C. and Jaboyedoff, M. (2012) Ambient seismic noise monitoring of a clay landslide: toward failure prediction. *Journal of Geophysical Research*, 117(F1), F01030. https://doi.org/10.1029/2011JF002159.

Mainsant, G., Chambon, G., Jongmans, D., Larose, E. and Baillet, L. (2015) Shear-wave-velocity drop prior to clayey mass movement in laboratory flume experiments. *Engineering Geology*, 192, 26–32. https://doi.org/10.1016/j.enggeo.2015.03.019.

Merritt, A.J., Chambers, J.E., Murphy, W., Wilkinson, P.B., West, L.J., Uhlemann, S., Meldrum, P.I. and Gunn, D. (2018) Landslide activation behaviour illuminated by electrical resistance monitoring. *Earth Surface Processes and Landforms*, 43(6), 1321–1334. https://doi.org/10.1002/esp.4316.

Musy, A. and Soutter, M. (1991) Physique du sol. *Presses polytechniques et universitaires romandes*, Lausanne, Switzerland.

Palis, E., Lebourg, T., Vidal, M., Levy, C., Tric, E. and Hernandez, M. (2017) Multiyear time-lapse ERT to study short- and long-term

landslide hydrological dynamics. *Landslides*, 14(4), 1333–1343. https://doi.org/10.1007/s10346-016-0791-6.

Paolella, M.S. (2019) *Linear Models and Time-Series Analysis. Regression, ANOVA, ARMA and GARCH*. Wiley Series in Probability and Statistics. John Wiley & Sons.

Rücker, C., Günther, T. and Spitzer, K. (2006) Three-dimensional modelling and inversion of DC resistivity data incorporating topography – I. Modelling. *Geophysical Journal International*, 166(2), 495–505. https://doi.org/10.1111/j.1365-246X.2006.03010.x.

Rücker, C., Günther, T. and Wagner, F.M. (2017) pyGIMLi: an open-source library for modelling and inversion in geophysics. *Computers & Geosciences*, 109, 106–123. https://doi.org/10.1016/j.cageo.2017.07.011.

Schütze, C., Friedel, S. and Jacobs, F. (2002) Detection of three-dimensional transport processes in porous aquifers using geoelectrical quotient tomography. *European Journal of Environmental and Engineering Geophysics*, 7, 03–19.

Supper, R., Ottowitz, D., Jochum, B., Kim, J.-H., Römer, A., Baron, I., Pfeiler, S., Lovisolo, M., Gruber, S. and Vecchiotti, F. (2014) Geoelectrical monitoring: an innovative method to supplement landslide surveillance and early warning. *Near Surface Geophysics*, 12(1), 133–150. https://doi.org/10.3997/1873-0604.2013060. URL https://www.earthdoc.org/content/journals/10.3997/1873-0604.2013060.

Telford, W.M., Geldart, L.P. and Sheriff, R.E. (1990) *Applied Geophysics*, 2nd edition. Cambridge University Press.

Travelletti, J., Sailhac, P., Malet, J.-P., Grandjean, G. and Ponton, J. (2012) Hydrological response of weathered clay-shale slopes: water infiltration monitoring with time-lapse electrical resistivity tomography. *Hydrological Processes*, 26(14), 2106–2119. https://doi.org/10.1002/hyp.7983.

Uhlemann, S., Wilkinson, P.B., Chambers, J.E., Maurer, H., Merritt, A.J., Gunn, D.A. and Meldrum, P.I. (2015) Interpolation of landslide movements to improve the accuracy of 4D geoelectrical monitoring. *Journal of Applied Geophysics*, 121, 93–105. https://doi.org/10.1016/j.jappgeo.2015.07.003.

Uhlemann, S., Chambers, J., Wilkinson, P., Maurer, H., Merritt, A., Meldrum, P., Kuras, O., Gunn, D., Smith, A. and Dijkstra, T. (2017) Four-dimensional imaging of moisture dynamics during landslide reactivation. *Journal of Geophysical Research: Earth Surface*, 122(1), 398–418. https://doi.org/10.1002/2016JF003983.

Waxman, M.H. and Smits, L.J.M. (1968) Electrical conductivities in oil-bearing shaly sands. *Society of Petroleum Engineering Journal*, 8, 107–122.

Whiteley, J.S., Chambers, J.E., Uhlemann, S., Wilkinson, P.B. and Kendall, J.M. (2019) Geophysical monitoring of moisture-induced landslides: a review. *Reviews of Geophysics*, 57(1), 106–145. https://doi.org/10.1029/2018RG000603.

Whiteley, J.S., Chambers, J.E., Uhlemann, S., Boyd, J., Cimpoiasu, M.O., Holmes, J.L., Inauen, C.M., Watlet, A., Hawley-Sibbett, L.R., Sujitapan, C., Swift, R.T. and Kendall, J.M. (2020) Landslide monitoring using seismic refraction tomography – The importance of incorporating topographic variations. *Engineering Geology*, 268, 105525. https://doi.org/10.1016/j.enggeo.2020.105525.

Wilkinson, P.B., Chambers, J.E., Meldrum, P.I., Gunn, D.A., Ogilvy, R.D. and Kuras, O. (2010) Predicting the movements of permanently installed electrodes on an active landslide using time-lapse geoelectrical resistivity data only. *Geophysical Journal International*, 183(2), 543–556. https://doi.org/10.1111/j.1365-246X.2010.04760.x.

Wilkinson, P.B., Uhlemann, S., Chambers, J.E., Meldrum, P.I. and Loke, M.H. (2015) Development and testing of displacement inversion to track electrode movements on 3-D electrical resistivity tomography monitoring grids. *Geophysical Journal International*, 200(3), 1566–1581. https://doi.org/10.1093/gji/ggu483.

Yeh, T.-C.J., Liu, S., Glass, R.J., Baker, K., Brainard, J.R., Alumbaugh, D. and LaBrecque, D. (2002) A geostatistically based inverse model for electrical resistivity surveys and its applications to vadose zone hydrology. *Water Resources Research*, 38(12), 1278. https://doi.org/10.1029/2001WR001204.